

High-speed phase-encoded quantum secure direct communication over 11.4 km heterogeneous free-space and fiber links

Ze-Zhou Sun^{1,2,*}, Yuan-Bin Cheng^{1,2,*}, Yu-Chen Liu^{1,2,*}, Jianxing Guo¹,
Xiao-Tian Song¹, Wei Zhang¹, Dong Pan^{1,†} and Gui-Lu long^{1,2,3,4,†}

¹Beijing Academy of Quantum Information Sciences, Beijing 100193, China

²State Key Laboratory of Low-dimensional Quantum Physics and Department of Physics,
Tsinghua University, Beijing 100084, China

³Frontier Science Center for Quantum Information, Beijing 100084, China

⁴Beijing National Research Center for Information Science and Technology, Beijing 100084, China

[†]Corresponding authors' email: pandong@baqis.ac.cn; gllong@mail.tsinghua.edu.cn

*These authors contributed equally to this work

Robust quantum transmission is driving a new paradigm in space-ground quantum networking. Although phase encoding has been widely adopted in terrestrial fiber channels, it has long been considered unsuitable for free-space quantum communication. Here, we demonstrate phase-encoded quantum communication over 1400 m of urban free space. The system maintained stable operation for nearly one hour, achieving 99.07% interference visibility and an average quantum bit error rate of 2.38%. The free-space quantum states were directly coupled into the fiber and transmitted over an additional 10 km, confirming seamless interoperability across different media. We further show that turbulence-induced

phase drifts between successive picosecond pulses can be effectively compensated. A cascaded-link model and numerical simulations indicate feasibility over free-space distances exceeding 30 km, underscoring the potential for satellite-to-ground quantum links. This work establishes the viability of phase encoding in free-space quantum networks, simplifying cross-medium integration and enabling compatibility with existing classical infrastructures.

A variety of quantum encoding schemes—including polarization, phase, time-bin, and quadrature of light—have been proposed and successfully demonstrated for quantum communication (1–5). Among them, polarization encoding has been most widely employed in free-space links due to its simplicity and the intrinsic stability of polarization states in atmospheric channels (6–10). However, polarization mode dispersion, birefringence, and depolarization fundamentally limit its performance in optical fibers. By contrast, time-bin and phase encoding are widely used in single-mode fiber networks, where they offer high stability, yet phase encoding is often deemed unsuitable for free-space transmission. If phase encoding were feasible in free space, it could greatly simplify infrastructure and reduce costs.

However, phase encoding in free-space channels faces three major challenges. First, the polarization of photonic states may drift, necessitating both active and passive compensation, while the complexity of atmospheric channels further aggravates phase instability. Second, turbulence-induced spatial perturbations disrupt temporal-mode measurements (11). Third, link-loss fluctuations degrade interference visibility (12). As quantum communication advances toward satellite-to-ground links, achieving high interference visibility remains a critical challenge (13).

The transmission loss, decoherence, and noise mechanisms of quantum states vary markedly across physical media, making cross-medium interconnection a persistent challenge. While free-space and fiber channels each offer distinct advantages, existing quantum communication systems remain dominated by point-to-point links tailored to specific encodings. The absence of architectures that seamlessly span different media has hindered large-scale quantum internet deployment and created an urgent demand for universal solutions. The inherently low energy of quantum states, the limited performance of current devices, and the short transmission windows of space-based links (14) place efficient use of quantum resources at the center of research. Recent strategies emphasize resource reuse through multifunctional integration, such as combining quantum key

distribution (QKD) with quantum time synchronization (15) and exploiting the same photon states for quasi quantum secure direct communication (QSDC) and QKD (16). These approaches open new pathways to enhance resource efficiency at the protocol layer of quantum networks (17–19).

Here we present a hybrid free-space–fiber quantum communication system based on a 1.25-GHz weak coherent light source with pure phase modulation. The system enables nearly one hour of continuous and stable transmission over 1.4 km of urban free space and 10 km of optical fiber. High interference visibility and low quantum bit error rates are maintained for four-phase-encoded states, defying the conventional expectation that atmospheric turbulence severely disrupts phase stability. A one-way quasi-QSDC (16) is achieved with a communication rate of 4.22 kbps. The encoding’s compatibility with fiber backends reduces network heterogeneity and system complexity, while the patch-cord optical interface extends the trusted boundary from telescope to internal devices, enhancing both security and deployment flexibility. Finally, we establish a qubit transmission model for this cross-media architecture, providing a theoretical foundation for future space–ground quantum networks.

Methods

The running protocol. We implement the simultaneous transmission of information and key exchange (STIKE) protocol (16) using four-phase encoding with Faraday–Sagnac–Michelson interferometers. The protocol comprises three main steps: (1) Encoding and preparation. To transmit quantum information between two distant parties, conventionally Alice and Bob, Alice first preprocesses the message using forward error correction, spread-spectrum coding, one-time-pad encryption, and masking. The resulting codewords are then encoded into quantum states, and photons are sent to Bob. (2) Measurement and security check. Upon receiving the photon sequence, Bob randomly selects measurement bases (Z or X) for each photon and publicly announces the corresponding timestamps and basis choices. A subset of basis-matched events is then jointly sampled to calculate the quantum bit error rate (QBER). If the QBER is below a predetermined threshold, the transmission is considered secure, and the protocol proceeds (20). (3) Decoding and post-processing. Both parties retain only the events measured in the same basis. Bob then performs three operations: (i) sequential unmasking, decryption, disspreading, and error-correction

decoding to recover Alice’s message, realizing quasi-QSDC; (ii) extraction of raw keys from the retained photons and Alice’s codewords for QKD, generating fresh encryption keys for subsequent quasi-QSDC sessions; (iii) recovery of keys associated with lost or discarded photons, enabled by channel monitoring and masking, allowing full recycling of consumed keys.

Relevant performance metrics, including the QBER, secure communication rate C_s , key consumption rate, key generation rate, and the percentage of key recycling P_{rec} , are recorded in real time during transmission by dedicated software. The key consumption rate is the rate at which keys are consumed for the retained photons. The percentage of key recycling refers to the fraction of keys recovered relative to the total number consumed in the encrypted codewords, and is theoretically given by $P_{\text{rec}} = 1 - Q_\mu/2$ in the absence of eavesdropping, where Q_μ denotes the gain of the signal states.

System details. Fig. 1 shows the experimental setup and environment. A 1.4 km free-space channel was established across an urban lake in Hefei, China, between the transmitter (Alice) at (31°53'36.4"N, 117°09'54.7"E) and the receiver (Bob) at (31°54'18.6"N, 117°09'38.5"E). Photons arriving at Bob were coupled into a 10 km optical fiber using a passive telescope system with a 120 mm entrance pupil, 27.1 \times magnification, a total focal length of 395 mm, and an optical path length of 330 mm. A triplet fiber-optic collimator was employed for efficient free-space–fiber coupling. Experiments were performed under two representative atmospheric conditions: (i) evening of May 26, 2025, wind level 2, 23°C, 60% humidity, visibility 24.1 km; and (ii) early morning of May 28, 2025, wind level 1, 29°C, 40% humidity, visibility 14 km.

Alice employs a 1.25 GHz laser with a pulse width of 50 ps and a central wavelength of 1549.32 nm to generate weak coherent pulses. An intensity modulator (IM), driven by a field-programmable gate array, modulates the laser output by applying pulse voltages of varying amplitudes, producing signal states ($\mu = 0.71$), decoy states ($\nu_1 = 0.28$), and vacuum states ($\nu_2 = 0$) in a ratio of 30:2:1. The IM is connected to a Faraday–Sagnac–Michelson interferometer with unequal arms via a circulator to perform encoding at the transmitter. Two cascaded phase modulators (PMs) randomly modulate phases of {0 or $\pi/2$ } and {0 or π } respectively according to the transmitted information, thereby enabling random four-phase modulation through their combination. After passing through the transmitting Faraday–Sagnac–Michelson interferometer loop, each pulse is split into two pulses separated by 400 ps and wavelength-division multiplexed with a 500 kHz clock



Figure 1: Schematic of our experimental setup featuring a 1.4 km free-space atmospheric channel over a lake surface combined with a 10 km optical fiber link in Hefei, China. IM, intensity modulator; CIR, circulator; BS, beam splitter; FM, Faraday mirror; PBS, polarization beam splitter; FR, Faraday rotator; PM, phase modulator; ATT, attenuator; VOA, variable optical attenuator; SPD, single photon detector; WDM, wavelength division multiplexer; SL, synchronization laser; APD, avalanche photon diode.

synchronization signal, which has a central wavelength of 1550.92 nm. Alice and Bob perform authenticated classical communication via a wireless Wi-Fi bridge. Bob employs a dual-channel InGaAs/InP single-photon detector (SPD) to detect photons. The detector operates at 1.25 GHz with a detection efficiency of 20%, a dark count rate of 1×10^{-6} , and an afterpulse probability of 1%. The inherent optical loss at Bob's receiving end is 6.5 dB. The system adopts a frame-by-frame transmission scheme to facilitate reliable communication. Each frame consists of 125 bytes and is transmitted with a spreading ratio of 1:1920, enhancing transmission robustness under varying channel loss conditions.

Results

In Fig. 2, we report the measured interference visibility and QBER during transmission, with the corresponding channel loss provided in Extended Data Fig. S1. The average visibilities over the two-day experiment reached 98.38% and 99.07%, respectively, comparable to state-of-the-art fiber-based

quantum communication (21, 22). These results confirm the feasibility of phase-encoded quantum transmission over both optical fiber and free-space channels. Notably, the interference visibility significantly surpasses that of previous free-space demonstrations (23–25), despite the increased number of transmitted quantum states and the longer free-space distance (Extended Data Fig. S2). During intervals when QBER temporarily exceeded 5%, interference visibilities were actively scanned to verify device integrity, meaning that the reported values represent a conservative lower bound. On the first day, the free-space link exhibited pronounced instability, with extreme QBER fluctuations and eventual transmission failure caused by the absence of an acquisition, pointing, and tracking (APT) system. By contrast, the second day demonstrated uninterrupted long-distance operation, where our built-in phase compensation mechanism effectively restored robustness against environmental turbulence.

Hence, we demonstrate that 1.25-GHz phase-encoded quantum states can withstand turbulence-induced phase drifts through active compensation. Detector counts yield the interference visibility, from which the actual phase difference is obtained. Comparing this with the ideal value provides the voltage offset associated with phase drift, which is subsequently applied to the ideal phase setting to realize dynamic feedback compensation. This robustness arises because the typical timescale of turbulence-induced fluctuations (0.01–0.1 s (26)) is orders of magnitude longer than the 400 ps separation between adjacent pulses. Consequently, consecutive pulses encoding the relative phase experience nearly identical atmospheric conditions, and the slowly varying turbulence has only a negligible impact on phase stability. Coupling the free-space signal into single-mode fibers further mitigates spatial perturbations via spatial-mode filtering, which can be enhanced with adaptive optics. Moreover, adopting a one-way protocol (16) reduces overall system loss compared with the two-way scheme (23), while independent suppression of channel-loss fluctuations ensures link stability. Together, these measures enable the phase-encoding system to sustain high and stable interference visibility under atmospheric turbulence.

Fig. 3 illustrates the transmission performance of the STIKE protocol. As the overall channel losses were comparable on the two experimental days (see Extended Data Fig. S1 in the Supplementary Information), the system achieved similar communication rates of 4.22 kbps and 3.90 kbps, with corresponding key consumption rates of 21.18 kbps and 27.68 kbps. A comparison with Figs. 2 and 3 reveals that during intervals of rapidly increasing QBER, the communication rate

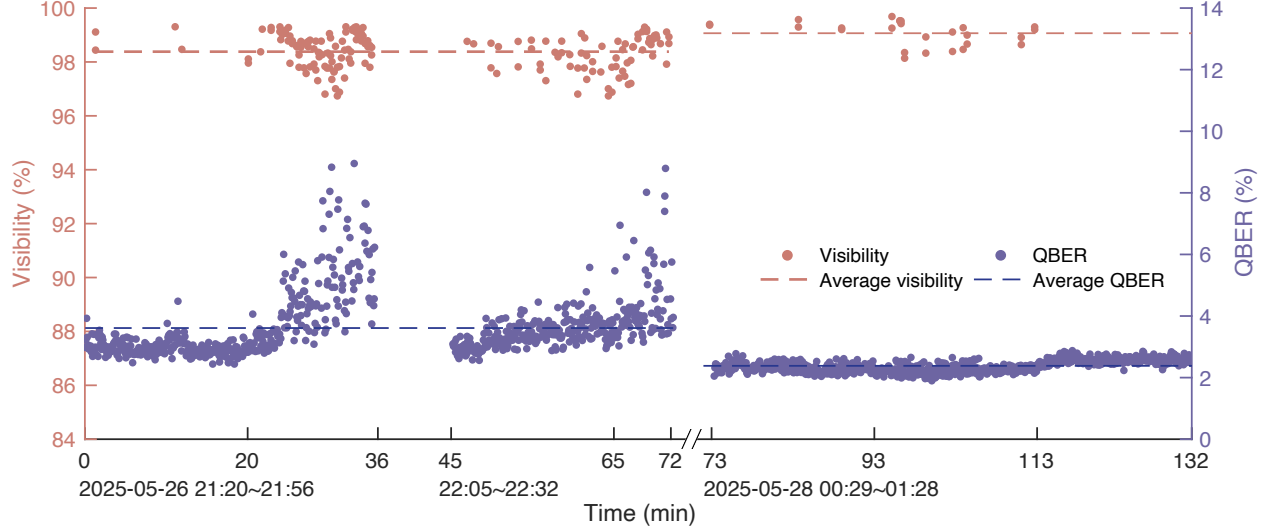


Figure 2: Interference visibility and QBER as functions of time. The average QBERs over the two experimental days were 3.61% and 2.38%, respectively. On the first day of operation the beam deviated from alignment at the 36th minute causing a link disconnection. The optical path was successfully recalibrated, which restored communication at the 45th minute.

points become noticeably sparse and the key generation rate gradually declines. This behavior is consistent with the degradation of link quality in the absence of an APT system. Consequently, poor link quality reduces the number of valid communication rate points. Under conditions of strong atmospheric turbulence, the system operated with a key generation rate of 13.51 kbps, which was lower than the consumption rate of 21.18 kbps, leading to a deficit of 7.67 kbps in the key pool. By contrast, during the second day, the channel remained stable with relatively steady QBER, enabling the system to achieve a key generation rate of 30.42 kbps, surpassing the consumption rate of 27.68 kbps and yielding a net surplus of 2.74 kbps for key pool replenishment. Over the two days, the system achieved average key recycling efficiencies of 99.9% and 99.97%, respectively, in excellent agreement with the theoretical prediction of $1 - Q_\mu/2$.

Fig. 4 presents the simulated rate bounds alongside our experimental results for the STIKE protocol over a hybrid fiber-free-space channel. Details of the simulation model are provided in the Supplementary Information. The fiber link was set to 10 km, which is representative of practical local-area transmission and can be adjusted as required. The results indicate that the key generation rate of our system is already close to the theoretical limit, whereas the communication

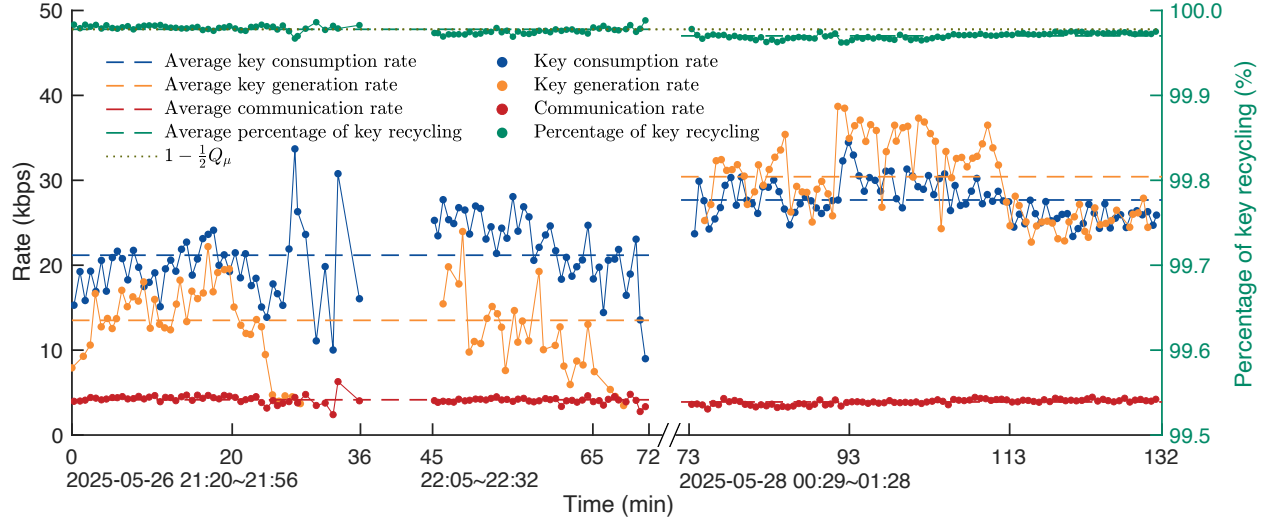


Figure 3: Transmission performance versus time. The average communication rates over the two days were 4.22 kbps and 3.90 kbps, the average key generation rates were 13.51 kbps and 30.42 kbps, the average key consumption rates were 21.18 kbps and 27.68 kbps, and the average key recovery percentages were 99.98% and 99.97%, respectively.

rate still falls short of the corresponding bound. To mitigate rapid fluctuations in the free-space channel loss, we employed a large spreading factor, with the resulting coding redundancy inevitably reducing the communication rate. This highlights the trade-off between accommodating channel-loss variations and maintaining communication efficiency in free-space links. As shown in Fig. 3, a relatively stable communication rate was nevertheless achieved under the larger spreading factor. Moreover, the simulation results suggest that the proposed cascaded transmission architecture holds strong potential for satellite–ground interactive quantum communication, as indicated by the dashed curves. Free-space transmission over more than 30 km exceeds the effective thickness of the atmosphere.

Discussion and outlook

We developed a four-phase-encoded quantum state transmission system based on a Faraday-Sagnac-Michelson interferometer and, for the first time, experimentally demonstrated stable quasi-QSDC over hybrid long-distance free-space and fiber channels, achieving both high interference visibility

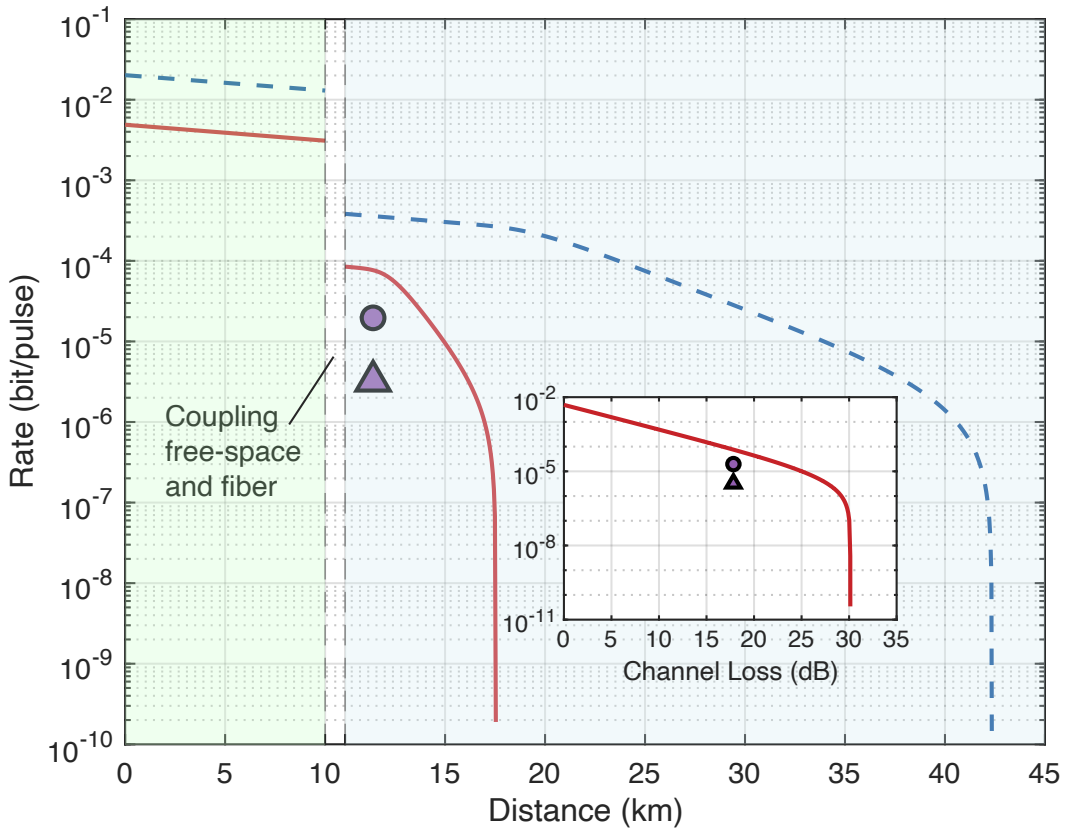


Figure 4: Simulation (lines) and experimental (symbols) results for the rate. The triangular and circular markers indicate the experimental communication rate and key generation rate, respectively. The solid curve shows the relationship between rate and distance derived from our experimental parameters. The dotted curve is calculated using a detector efficiency of 80%, a telescope system conversion efficiency of $10^{-15.4/10}$, and a receiving telescope aperture of 1 m.

and low QBER. Our results extend free-space QSDC from meter-scale laboratory demonstrations to the kilometer scale under urban atmospheric conditions, achieving a record transmission rate of 4.22 kbps. This represents an eightfold improvement in transmission rate and a 140-fold extension in distance compared with existing free-space QSDC implementations (23). These advances demonstrate the feasibility of QSDC for transmitting text, images, and real-time voice over free-space channels.

The STIKE protocol operates flexibly in multiple modes according to channel conditions and communication requirements. It can sustain secure communication by allocating no codeword space to random numbers when self-sufficiency in key generation is achieved, or by allocating a portion of the codeword to random numbers when key consumption exceeds key generation, a feature that is particularly important under prolonged adverse link conditions.

The constructed system exhibits notable advantages in resource efficiency, architectural simplicity, and reduced device heterogeneity, while also demonstrating excellent scalability and practical potential for space–ground integrated network deployment. This design enables a single quantum communication device to operate seamlessly across both free space and fiber channels, allowing plug-and-play switching between them and thus realizing cross-medium multiplexing of communication hardware. Furthermore, the phase-encoded architecture is inherently compatible with chip-level integration (27, 28), since on-chip propagation naturally preserves phase information and requires lower power consumption. The preparation, transmission, and interference measurement of qubits based on the phase difference between consecutive pulses form the essential infrastructure for quantum communication (29–31), distributed optical quantum computing (32–34), and quantum sensing (24, 35). Our results are expected to provide a universal architecture for cross-medium, long-distance quantum information transmission, paving the way toward integrated quantum information processing networks (36).

References and Notes

1. S. Lloyd, *et al.*, Infrastructure for the quantum Internet. *ACM SIGCOMM Computer Communication Review* **34** (5), 9–20 (2004).
2. H. J. Kimble, The quantum internet. *Nature* **453** (7198), 1023–1030 (2008).
3. S. Wehner, D. Elkouss, R. Hanson, Quantum internet: a vision for the road ahead. *Science* **362** (6412), eaam9288 (2018).
4. G.-L. Long, *et al.*, An evolutionary pathway for the quantum internet relying on secure classical repeaters. *IEEE Network* **36** (3), 82–88 (2022).
5. D. Pan, *et al.*, The evolution of quantum secure direct communication: on the road to the qinternet. *IEEE Communications Surveys & Tutorials* **26** (3), 1898–1949 (2024).
6. W. Buttler, *et al.*, Free-space quantum-key distribution. *Physical Review A* **57** (4), 2379 (1998).
7. T. Schmitt-Manderbach, *et al.*, Experimental demonstration of free-space decoy-state quantum key distribution over 144 km. *Physical Review Letters* **98** (1), 010504 (2007).
8. G. Vallone, *et al.*, Experimental satellite quantum communications. *Physical Review Letters* **115** (4), 040502 (2015).
9. W. Zhang, *et al.*, Quantum secure direct communication with quantum memory. *Physical Review Letters* **118** (22), 220501 (2017).
10. M. Avesani, *et al.*, Full daylight quantum-key-distribution at 1550 nm enabled by integrated silicon photonics. *npj Quantum Information* **7** (1), 93 (2021).
11. J. Jin, *et al.*, Demonstration of analyzers for multimode photonic time-bin qubits. *Physical Review A* **97** (4), 043847 (2018).
12. A. T. Castillo, U. Zanforlin, G. Buller, R. Donaldson, Multiprotocol quantum key distribution receiver for free space, in *Quantum Technology: Driving Commercialisation of an Enabling Science III* (SPIE), vol. 12335 (2023), pp. 79–83.

13. G. Vallone, *et al.*, Interference at the single photon level along satellite-ground channels. *Physical Review Letters* **116** (25), 253601 (2016).
14. R. Bedington, J. M. Arrazola, A. Ling, Progress in satellite quantum key distribution. *npj Quantum Information* **3** (1), 30 (2017).
15. X. Xiang, *et al.*, Towards a Function-Scalable Quantum Network With Multiplexed Energy-Time Entanglement. *Laser & Photonics Reviews* p. e00658 (2025).
16. D. Pan, *et al.*, Simultaneous transmission of information and key exchange using the same photonic quantum states. *Science Advances* **11** (8), eadt4627 (2025).
17. Y. Cao, *et al.*, The evolution of quantum key distribution networks: On the road to the qinternet. *IEEE Communications Surveys & Tutorials* **24** (2), 839–894 (2022).
18. J. Illiano, M. Caleffi, A. Manzalini, A. S. Cacciapuoti, Quantum internet protocol stack: A comprehensive survey. *Computer Networks* **213**, 109092 (2022).
19. Z.-Z. Sun, *et al.*, Quantum communication network routing with circuit and packet switching strategies. *IEEE Journal on Selected Areas in Communications* **43** (5), 1887–1900 (2025), doi:10.1109/JSAC.2025.3543524.
20. C. Wang, Quantum secure direct communication: Intersection of communication and cryptography. *Fundamental Research* **1** (1), 91–92 (2021), doi:<https://doi.org/10.1016/j.fmre.2021.01.002>.
21. B. Korzh, *et al.*, Provably secure and practical quantum key distribution over 307 km of optical fibre. *Nature Photonics* **9** (3), 163–168 (2015).
22. S. Wang, *et al.*, Practical gigahertz quantum key distribution robust against channel disturbance. *Optics Letters* **43** (9), 2030–2033 (2018).
23. D. Pan, *et al.*, Experimental free-space quantum secure direct communication and its security analysis. *Photonics Research* **8** (9), 1522–1531 (2020).
24. S. Saeed, T. Jennewein, Observing quantum coherence from photons scattered in free-space. *Light: Science & Applications* **10** (1), 121 (2021).

25. S. Cocchi, *et al.*, Time-bin encoding quantum key distribution in free-space horizontal links during nighttime and daytime. *Optica Quantum* **3** (4), 346–350 (2025).
26. N. Gisin, G. Ribordy, W. Tittel, H. Zbinden, Quantum cryptography. *Reviews of Modern Physics* **74** (1), 145 (2002).
27. W. Luo, *et al.*, Recent progress in quantum photonic chips for quantum communication and internet. *Light: Science & Applications* **12** (1), 175 (2023).
28. L.-C. Kwek, *et al.*, Chip-based quantum key distribution. *AAPPS Bulletin* **31** (1), 15 (2021).
29. K. Inoue, E. Waks, Y. Yamamoto, Differential phase shift quantum key distribution. *Physical Review Letters* **89** (3), 037902 (2002).
30. H. Yu, A. O. Govorov, H.-Z. Song, Z. Wang, Time-encoded photonic quantum states: generation, processing, and applications. *Applied Physics Reviews* **11** (4) (2024).
31. J. Wang, *et al.*, Time-bin encoded quantum key distribution over 120 km with a telecom quantum dot source. *arXiv preprint arXiv:2506.15520* (2025).
32. P. C. Humphreys, *et al.*, Linear optical quantum computing in a single spatial mode. *Physical Review Letters* **111** (15), 150501 (2013).
33. X. Liu, *et al.*, Nonlocal photonic quantum gates over 7.0 km. *Nature Communications* **15** (1), 8529 (2024).
34. P. Rübeling, R. Johanning, J. Heine, O. V. Marchukov, M. Kues, Fiber transmission of cluster states via multi-level time-bin encoding. *arXiv preprint arXiv:2507.01497* (2025).
35. W. He, *et al.*, Experimental secure entanglement-free quantum remote sensing over 50 km of optical fiber. *Physical Review A* **111** (6), 062607 (2025).
36. Y.-R. Fan, *et al.*, Quantum entanglement network enabled by a state-multiplexing quantum light source. *Light: Science & Applications* **14** (1), 189 (2025).
37. I. Karakosta-Amarantidou, R. Yehia, M. Schiavon, Free-space model for a balloon-based quantum network. *Physical Review Research* **7** (2), 023199 (2025).

38. J.-P. Bourgoin, *et al.*, Free-space quantum key distribution to a moving receiver. *Optics Express* **23** (26), 33437–33447 (2015).
39. D. Vasylyev, A. Semenov, W. Vogel, Atmospheric quantum channels with weak and strong turbulence. *Physical Review Letters* **117** (9), 090501 (2016).
40. R. L. Fante, Electromagnetic beam propagation in turbulent media. *Proceedings of the IEEE* **63** (12), 1669–1692 (2005).
41. M. Ghalaii, S. Pirandola, Quantum communications in a moderate-to-strong turbulent space. *Communications Physics* **5** (1), 38 (2022).
42. A. Trichili, M. A. Cox, B. S. Ooi, M.-S. Alouini, Roadmap to free space optics. *Journal of the optical society of America B* **37** (11), A184–A201 (2020).

Acknowledgments

We acknowledge support by the National Natural Science Foundation of China (No. 12205011 and No. 11974205), the Young Elite Scientists Sponsorship Program by CAST (No. YESS20240786), Tsinghua University Initiative Scientific Research Program, and Beijing Advanced Innovation Center for Future Chip (ICFC).

Author contributions: D.P. and G.-L.L. supervised and conceived the work. Z.-Z.S., Y.-B.C., Y.-C.L., D.P., and G.-L.L. designed and performed the experiments. Z.-Z.S., D.P, and Y.-B.C. analysed the experimental data and constructed the channel model. D.P. and J.G. designed the software. X.-T.S. and W.Z. contributed to the preliminary experiments. Z.-Z.S., D.P., and G.-L.L. wrote the paper with contributions from all authors. All authors discussed the results.

Competing interests: The authors declare no competing interests.

Data and materials availability: Correspondence and requests for materials should be addressed to Dong Pan and Gui-Lu Long.

Supplementary materials

Secrecy capacity in cross-medium transmission

Figs. S1 to S2

Tables S1 to S2

Supplementary Materials for High-speed phase-encoded quantum secure direct communication over 11.4 km heterogeneous free-space and fiber links

Ze-Zhou Sun^{1,2,*}, Yuan-Bin Cheng^{1,2,*}, Yu-Chen Liu^{1,2,*}, Jianxing Guo¹,

Xiao-Tian Song¹, Wei Zhang¹, Dong Pan^{1,†} and Gui-Lu long^{1,2,3,4,†}

¹Beijing Academy of Quantum Information Sciences, Beijing 100193, China

²State Key Laboratory of Low-dimensional Quantum Physics and Department of Physics,
Tsinghua University, Beijing 100084, China

³Frontier Science Center for Quantum Information, Beijing 100084, China

⁴Beijing National Research Center for Information Science and Technology, Beijing 100084, China

[†]Corresponding authors' email: pandong@baqis.ac.cn; gllong@mail.tsinghua.edu.cn

*These authors contributed equally to this work

This PDF file includes:

Secrecy capacity in cross-medium transmission

Figs. S1 to S2

Tables S1 to S2

Secrecy capacity in cross-medium transmission

Gaussian beams are employed to characterize the spatial profile of weak coherent pulse sources, which sufficiently describe the link loss in free-space optical transmission and have been widely adopted in the Bennett-Brassard 1984 and entanglement distribution protocols (37,38). We employ the widely adopted metric, the Rytov number σ_{Ry}^2 , to quantify the turbulence intensity within a link (39). It characterizes the fluctuations in the received irradiance or in the phase and amplitude of the light as it propagates through turbulent media, with its definition given by

$$\sigma_{Ry}^2 = 1.23C_n^2k^{\frac{7}{6}}d_1^{\frac{11}{6}}, \quad (S1)$$

where $k = 2\pi/\lambda$ is the wavenumber, d_1 is the distance of free-space channel, and C_n^2 is the atmospheric index-of-refraction structure constant, which is used to quantify the refractive index variations caused by inhomogeneities in temperature, humidity, pressure, and other factors in the atmosphere. One parameter associated with photon propagation in turbulent channel is (40) $d_i = 1/(C_n^2 k^2 l_0^{5/3})$. It denotes the propagation length at which the transverse coherence radius of a light wave becomes comparable to the turbulence inner scale l_0 , which characterizes the smallest length scale over which refractive-index fluctuations remain correlated. As shown by the parameters in Table S1, d_i is approximately 475 km under our experimental conditions.

Assuming that the beam waist of Alice's weak coherent pulse is w_0 , the telescope magnification is Γ , and the light is collected by a receiver with a finite aperture of radius a_R . It has been proven that (41), in both weak and moderate-to-strong turbulence, provided the transmission distance d_1 is less than the critical propagation distance of d_i , the effective beam waist w_{d_1} becomes

$$w_{d_1} = w_0 \Gamma \sqrt{1 + \left(\frac{d_1}{d_R}\right)^2} \sqrt{1 + 1.63(\sigma_{Ry}^2)^{\frac{6}{5}} \Theta}, \quad (S2)$$

where $d_R = \pi w_0^2 \Gamma^2 / \lambda$ is the Rayleigh length of the beam, and Θ is defined as

$$\Theta = \frac{2d_1 d_R^2}{k w_0^2 \Gamma^2 (d_R^2 + d_1^2)}. \quad (S3)$$

Then, the total transmittance η for the entire link, which accounts for the free-space channel loss, conversion loss, fiber channel loss, the transmittance of receiving end η_B , and the detector efficiency η_D , can be expressed as (41)

$$\eta = (1 - e^{-\frac{2a_R^2}{w_{d_1}^2}}) 10^{-\frac{\alpha_1 d_1}{10}} 10^{-\frac{L_c}{10}} 10^{-\frac{\alpha_2 d_2}{10}} \eta_B \eta_D, \quad (S4)$$

where α_1 and α_2 respectively denote the attenuation coefficients of the free-space channel and the fiber channel, d_2 is the distance of fiber channel, and L_c is the conversion loss, which includes the loss associated with the transmitting telescope converting the optical signal in fiber into a spatial beam, and the receiving telescope coupling the spatial beam back into an optical fiber.

The secrecy capacity of the STIKE protocol based on the decoy-state method is given by (16)

$$C_s = qQ_\mu \left\{ -fH_2(E_\mu) + \frac{Q_1}{Q_\mu} [1 - H_2(e_1)] \right\}, \quad (S5)$$

where $H_2(x) = -x \log(x) - (1-x) \log(1-x)$ is the binary entropy function, $q = 1/2$, and f is the error correction efficiency. Furthermore, Q_μ and E_μ denote the total gain and QBER of the signal state, respectively, while Q_1 and e_1 represent the gain and QBER of the single-photon state. These quantities are expressed as follows:

$$\begin{aligned} Q_{\mu(\nu)} &= Y_0 + 1 - e^{-\eta\mu(\nu)}, \\ E_{\mu(\nu)}Q_{\mu(\nu)} &= e_0Y_0 + e_{\text{det}}(1 - e^{-\eta\mu(\nu)}), \\ Q_1 &= \frac{\mu^2 e^{-\mu}}{\mu\nu - \nu^2} (Q_\nu e^\nu - Q_\mu e^\mu \frac{\nu^2}{\mu^2} - \frac{\mu^2 - \nu^2}{\mu^2} Y_0), \\ e_1 &= \frac{\mu e^{-\mu} (E_\nu Q_\nu e^\nu - e_0 Y_0)}{\nu Q_1}, \end{aligned} \quad (S6)$$

where μ, ν are the average photon numbers of the signal state and the decoy state, respectively. Q_ν, E_ν are the total gain and QBER of the decoy state, and $Y_0 = 2p_d$ is the yield of a zero-photon state. $e_{\text{det}} = (1 - V)/2$ is the intrinsic detector error rate, where V is the interference visibility, and $e_0 = 1/2$ is the error rate of background. The quasi-QSDC and QKD in STIKE share the same information-theoretic security bound.

1 Parameters obtained from the experiment

Extended Data Fig. S1 shows the variation of the total channel loss L_t over time for the 1.4 km free-space link combined with 10 km of optical fiber during three 5-minute intervals. The first segment of loss data was obtained at the start of the first experiment, while the second and third segments were measured before and after the second transmission experiment, respectively. The total loss from the 10-km optical fiber and the fiber optic adapter is 2.42 dB. The maximum loss fluctuations across the three intervals are 2.72 dB, 3.17 dB, and 2.39 dB, respectively. The average total channel loss

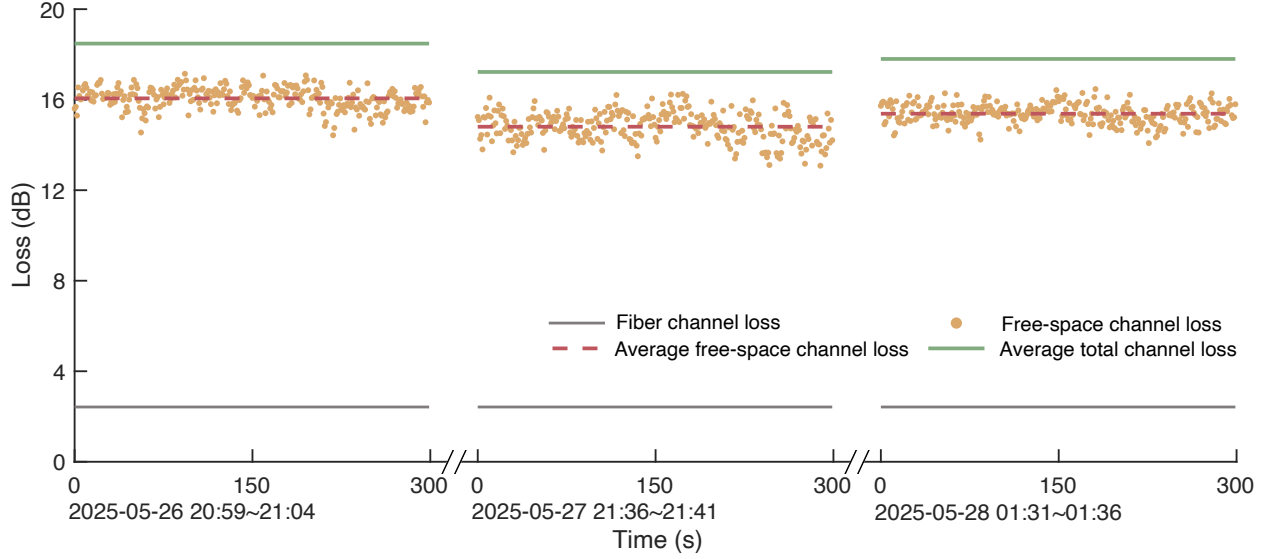


Figure S1: Temporal variation of total loss in the 1.4 km free-space and 10 km fiber hybrid channel. The channel loss of the 10-km fiber is 2 dB, and the loss of its associated fiber optic adapter is 0.42 dB. The total channel loss is the sum of the free-space channel loss and the fiber channel loss (2.42 dB).

over the two-day experiment was 18.48 dB and 17.51 dB, respectively. The relatively low average channel loss on the second day, together with the consistency of the loss measurements before and after the experiment, demonstrates the potential for our system to operate continuously for extended periods even without an APT system actively maintaining link quality. In free-space transmission of time-bin-encoded qubits, quantum states in the X basis intrinsically possess two distinct phases and are ultimately measured through interference. The system performance is therefore characterized by the interference visibility. We compare our results with two representative studies (24, 25), even if they are not pure phase-encoded qubit transmission over free-space channel, as shown in Extended Data Fig. S2. Extended Data Tables 1 and 2 summarize the measured experimental parameters and results, as well as the simulation parameters.

Table S1: Extended Data Table 1: Experimental parameters and results.

Description	Parameter	Value
Telephoto system magnification	Γ	27.1×
Receiver entrance pupil radius	a_R	60 mm
Error correction efficiency	f	1.22
Dark count rate of single-photon detector	p_d	1×10^{-6}
Internal transmittance at Bob's side	η_B	$10^{-6.5/10}$
Average photon number of signal state	μ	0.71
Average photon number of decoy state	ν	0.28
Detector efficiency	η_D	20%
Two-day average interference visibility	V	98.47%
Conversion loss	L_c	15.40 dB
Total channel loss	L_t	17.83 dB
QBER of signal state	E_μ	2.87%
QBER of decoy state	E_ν	4.01%
Signal-state gain	Q_μ	5.31×10^{-4}
Decoy-state gain	Q_ν	2.09×10^{-4}

Table S2: Extended Data Table 2: Simulation parameters.

Description	Parameter	Value
Emission beam waist	w_0	1.74 mm
Index-of-refraction structure constant	C_n^2	$1.28 \times 10^{-14} \text{ m}^{-\frac{2}{3}} (41)$
Turbulence inner scale	l_0	0.001 m (41)
Attenuation coefficient of free-space channel	α_1	0.2 dB/km (42)
Attenuation coefficient of fiber channel	α_2	0.2 dB/km

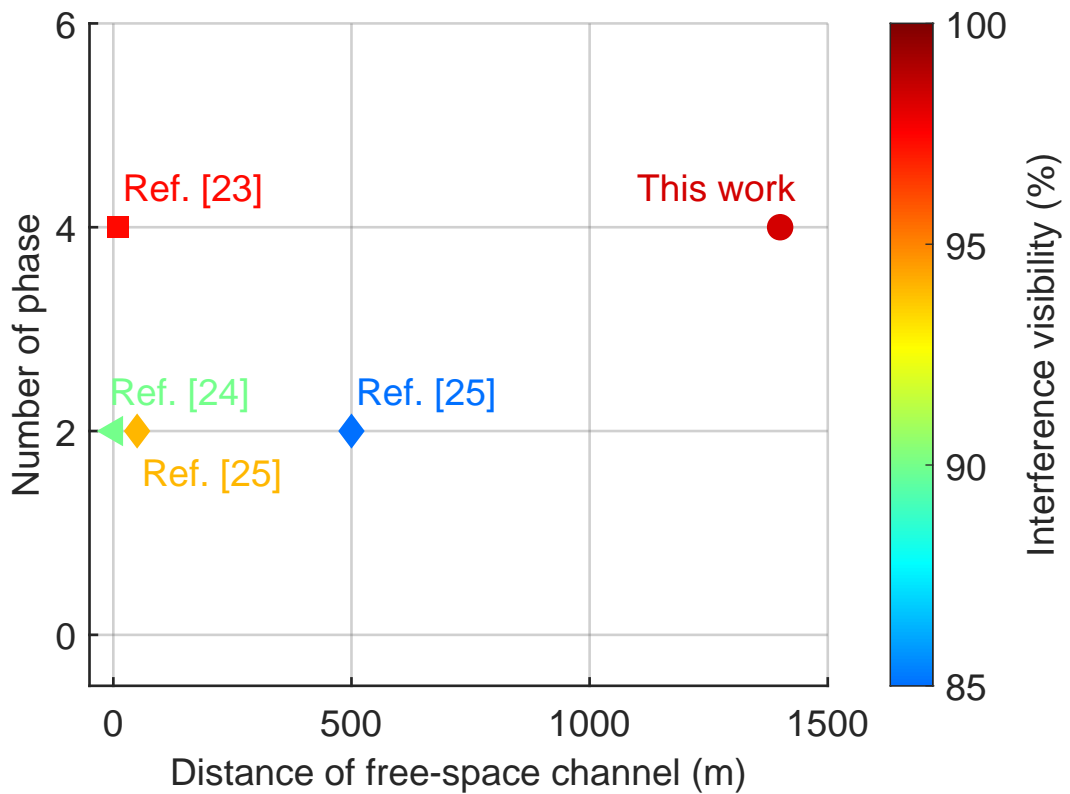


Figure S2: Interference visibility of our system compared with previous results (23–25), all without an APT system.